KFUPM
Journal of Undergraduate Research International

Diamond Open Access 164

Article Mechanical Engineering

Preliminary Run-to-Failure Characterization of UAV Propulsion Systems

Lujain Almuzaini and Mohammed A. A. Ismail*

Cite https://doi.org/10.64589/juri/231554

Submitted: April 25, 2026 **Revised:** May 11, 2026 **Accepted:** May 16, 2026

ABSTRACT

The expanding use of unmanned aerial vehicles (UAVs) across industrial, agricultural, and safety-critical applications in recent decades demands dependable operations and precise predictive capabilities under harsh environmental conditions. This study presents the design, instrumentation, and experimental validation of a run-to-failure testbed developed to replicate realistic UAV propulsion system stressors in controlled laboratory settings. The setup included a brushless DC (BLDC) motor, a propeller-mounted piezoelectric vibration accelerometer, motor current sensing, and active temperature regulation, allowing the simultaneous acquisition of multi-modal degradation signals across the propeller component lifecycle. Five run-to-failure experiments were conducted. The collected data were analyzed using two established predictive feature quality metrics, trendability and prognosability, to assess the degradation tracking potential of the vibration acceleration and motor current measurements. The results consistently show that the vibration root mean square (RMS) achieved Spearman trendability coefficients exceeding 0.85 across almost all five runs, compared to motor current RMS values that remained below 0.65, and vibration prognosability scores consistently surpassed 0.80, confirming a clear statistical separation between healthy and near-failure states. These results have practical implications for the development of condition-based maintenance strategies for UAV fleets, enabling operators to replace time-based inspection schedules with data-driven prognostic frameworks that reduce unplanned downtime and improve operational safety. The publicly available dataset addresses a critical gap in the prognostics literature and provides a foundation for the development and validation of data-driven remaining useful life estimation algorithms for UAV propulsion systems operating in arid environments.

Keywords: remaining useful life, propeller degradation, fault detection and diagnosis, run-to-failure testing, prognostics and health management, brushless DC motor, vibration-based condition monitoring

1. INTRODUCTION

The use of unmanned aerial vehicles (UAVs), commonly referred to as drones, has been rapidly adopted across multiple sectors in Saudi Arabia, including agriculture, healthcare, transportation, infrastructure inspection, and public safety. For example, the healthcare sector in Saudi Arabia has utilized drones to significantly improve emergency response times, extend medical assistance to remote areas, and alleviate pressure on overstretched medical infrastructure. These capabilities are particularly beneficial given the vast geographic area and dispersed population centers of the Kingdom [1]. Beyond healthcare, the Saudi UAV market is expected to grow substantially, reinforced by government investment in both defense and commercial drone development under the "Vision 2030 Economic Diversification Agenda" [2]. As drone utilization increases in time-sensitive operations, ensuring consistent operational reliability has evolved from a narrow engineering concern into a matter of national strategic importance. Component failures, particularly in propulsion systems, can cause operational delays, significant financial loss, and serious safety risks [3].

Propellers are among the most mechanically demanding components in multi-rotor drones. The primary lift and thrust generators operate under continuous aerodynamic stress while maintaining vehicle stability. Their exposure to consistent rotational loads, mechanical vibrations, and harsh environmental conditions, including extreme ambient temperatures and coarse debris particulates, which are common weather conditions on the Arabian Peninsula, accelerates structural wear. Critically, the loss of even a single actuator in an underactuated platform, such as a quadrotor, can result in an irreversible loss of controllability and vehicle crashes [4], with potentially severe safety and financial consequences in operations.

Estimating the remaining serviceable life before a propeller fails, known as its remaining useful life (RUL), is a fundamental requirement for cost-effective and uninterrupted UAV operation. Accurate RUL estimation allows operators to transition from scheduled maintenance to condition-based and predictive maintenance, thereby minimizing unplanned downtime. The severe lack of publicly available datasets that capture realistic, environmentally representative propulsion system degradation poses

Published under an exclusive license by KFUPM

a fundamental constraint on existing predictive approaches, regardless of advances in drone fault detection.

Addressing this gap, recent initiatives such as the PADRE repository have made important contributions by providing open datasets for propeller fault detection and classification in multi-rotor UAVs[5]. However, PADRE and comparable repositories were assembled under controlled laboratory conditions that do not reproduce the demanding stressors encountered in real-world applications. The DronePropA dataset[6] simulates propeller damage through deliberate physical modification, rather than natural degradation, which limits the generalizability of the model to real operational scenarios.

To address these limitations, this study presents the design, instrumentation, and experimental validation of a run-to-failure testbed specifically developed to generate naturalistic propulsion system degradation data under arid environmental conditions. The resulting datasets, which capture the complete degradation lifecycle from a healthy baseline to functional failure, are publicly available to support next-generation data-driven RUL estimation and fault detection research.

The remainder of this manuscript is organized as follows: Section II outlines the underlying material properties and methodology; Section III details the experimental program implementation; Section IV presents and analyzes the experimental results; and Section V provides the concluding remarks, study limitations, and suggestions for future work.

1.1. UAV Faults and Failures.

Faults in UAVs can be defined as abnormal system behavior, whereas failures represent permanent and irrecoverable corruption in the ability of the system to perform a task. Given that a fault may be transient or compensable, while a failure demands immediate intervention and typically results in mission abort or vehicle loss, the distinction is operationally important[7]. Both are categorized into four principal types: actuator, sensor, communication, and software. Each category has distinct implications for detection, isolation, and recovery[7]. The most operationally consequential faults and failures are the actuator and sensor faults. Actuator faults, such as propeller damage, motor degradation, and electronic speed controller (ESC) anomalies, disrupt thrust and torque generation. However, sensor faults corrupt the state estimation pipeline, potentially inducing erroneous control responses. The common fault types and their distributions are illustrated in Figure 1[8–10].

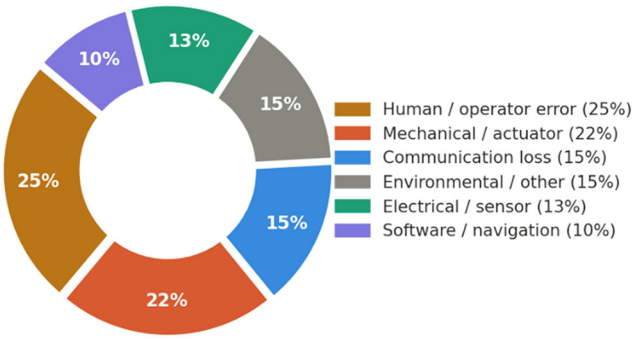

Figure 1. UAV fault type distribution by reported cause and common fault categories in multi-rotor platforms

1.2. Propeller Fault Characterization.

Propellers are vulnerable to structural damage from sustained exposure to environmental stressors, such as wind debris, high temperatures, and mechanical vibrations. Any change to the geometry, surface, or mass distribution of a propeller is a fault condition that compromises the aerodynamic performance and vehicle stability. These faults are broadly organized into four principal categories, as illustrated in Figure 2: fatigue, edge cuts, cracks, and surface imbalance[12,13].

Fatigue defects are caused by cyclic mechanical stress that gradually weakens the blade material without causing noticeable surface damage during the early stages. Edge cuts are defined as localized material losses along the leading or trailing edges, altering the pressure distribution, introducing asymmetric loading between paired propellers, and increasing drag. Cracks, whether transverse or longitudinal, reduce the blade stiffness and lift capacity. Furthermore, as the crack tip stress intensity factor approaches the fracture toughness, it is subjected to stress-driven propagation, which accelerates nonlinearly. Surface imbalance faults arise from an asymmetric mass distribution and produce a radial force imbalance that appears as an elevated vibration throughout the propulsion system[12].

1.3. Fault Detection and Diagnosis.

Fault detection and diagnosis (FDD) systematically characterizes faults based on their nature, location, and severity, forming the foundation of drone reliability assurance[4]. FDD methods are organized into three paradigms. Model-based approaches, such as Kalman filters and parity space analysis, perform well under well-characterized conditions but are less effective under environmental variability or nonlinear system behavior[4]. Data-driven methods, including neural networks and fuzzy logic systems, adapt to variable conditions without requiring an explicit dynamic model but depend on large volumes of high-quality labeled training data[6]. Hybrid approaches combine both the rigor of model-based methods with data-driven adaptability and are generally considered the most promising direction for robust UAV fault detection[7].

2. METHODOLOGY

The objective of this study is to evaluate the potential of vibration acceleration and motor current measurements for tracking propulsion system degradation in a run-to-failure experimental setting. Two established prognostic feature quality metrics, namely trendability and prognosability, were applied to the sensor data acquired during the controlled experiments. Both metrics operate on the root mean square (RMS) of each sensor signal computed per recording burst, providing a scalar representation of the signal energy, which changes with the structural condition of the propeller.

2.1. Data Collection.

The subject of this study was a drone propulsion system consisting of a brushless DC (BLDC) motor and a fixed propeller. A piezoelectric accelerometer was mounted on the motor frame to monitor mechanical vibrations. A current sensor was integrated into the motor supply circuit to track electrical performance. Throughout the entire degradation lifecycle, data were continually recorded during constant-speed

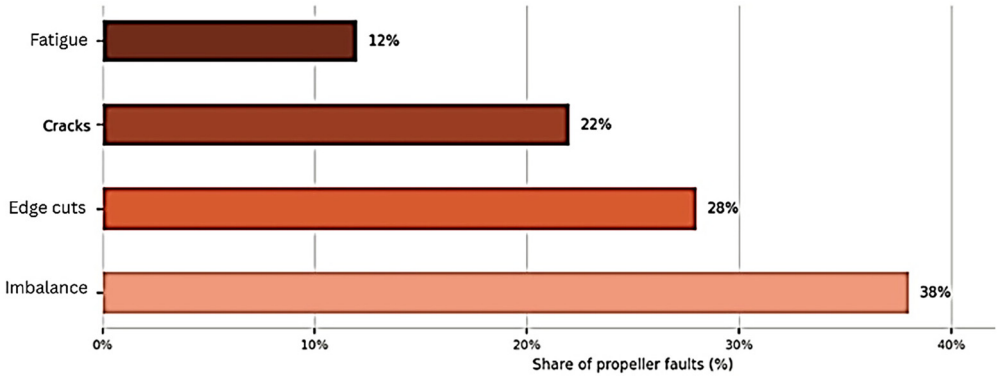

Figure 2. Propeller fault subtypes: fatigue, edge cuts, cracks, and surface imbalance

motor operation until natural propeller failure occurred, capturing both vibration acceleration and motor current. To guarantee diversity in failure modes and allow the statistical evaluation of measurement consistency between runs, five independent run-to-failure experiments were conducted on distinct propeller specimens. Each experiment was terminated when functional failure was detected, defined as an abrupt and irreversible increase in vibration amplitude exceeding three standard deviations above the running mean, accompanied by audible structural distress, indicating an imminent or actual fracture.

2.2. Prognostic Feature Quality Metrics.

2.2.1. Trendability. Trendability measures whether a health indicator follows a consistent and temporally ordered pattern throughout the failure progression process. It is evaluated using the Pearson and Spearman rank correlation coefficients computed between the segment-level RMS feature and elapsed operating time. Whereas the Pearson correlation quantifies the strength of a linear relationship, the Spearman rank correlation captures any monotonic relationship, including the nonlinear acceleration of the damage characteristic of the fracture mechanics-governed crack propagation. Formally, for a given run with N recording bursts, the RMS value for each burst k is computed as

$$x_{RMS} = \sqrt{\frac{1}{n}\sum_{i=1}^{n} x_i^2}, \tag{1}$$

where x_i represents the individual sensor samples and n = 50,000 is the number of samples per burst. The Pearson trendability is then calculated as

$$r_{Pearson} = \frac{\sum_{i=1}^{n}(x_i - \bar{x})(y_i - \bar{y})}{\sqrt{\sum_{i=1}^{n}(x_i - \bar{x})^2}\sqrt{\sum_{i=1}^{n}(y_i - \bar{y})^2}}, \tag{2}$$

where y_i is the elapsed time at burst i. The Spearman rank trendability $r_{Pearson}$ is computed identically, but on the rank-transformed values of x_i and y_i, thereby capturing monotonic nonlinear trends without assuming linearity. The final trendability score for each run was reported as the absolute value of the correlation coefficient, with values approaching 1.0 indicating a strong temporal ordering of the degradation feature [14,15].

2.2.2. Prognosability. Prognosability measures the statistical separability between the early and end-of-life RMS feature distributions. A feature with high prognosability produces a signal state near failure that is clearly and consistently distinguishable from its initial state, allowing the proximity to failure to be reliably identified. The prognosability metric is computed by comparing the distributions of RMS values from the initial operating phase (first 20% of the recording bursts) and the end-of-life phase (last 20% of the recording bursts) for each run. Specifically, prognosability P is defined as

$$P = \exp\left(-\frac{std\,(F_{EOL})}{\left|\overline{F_{EOL}} - \overline{F_{init}}\right|}\right), \tag{3}$$

where F_{init} and F_{EOL} denote the sets of RMS values from the initial and end-of-life phases, respectively, $std\,(F_{EOL})$ is the standard deviation of the end-of-life RMS values, and the denominator captures the absolute difference between the mean values of both phases. A prognosability score approaching 1.0 indicates that the end-of-life feature values are tightly clustered and well-separated from the initial values, enabling reliable failure proximity detection. Scores near zero indicate that the feature distributions overlap substantially, making the failure prediction unreliable. The metric was computed independently for each of the five runs to assess the cross-run consistency [16,17].

3. EXPERIMENTAL SECTION

3.1. Test Setup and Instrumentation. The experimental setup is listed in Table 1 and was assembled as shown in Figures 3 and 4. The BLDC motor, which drives the propeller, was fixed to a stable frame to isolate the vibrations generated by external noise. A piezoelectric accelerometer (Metra KS48C) was mounted directly on the motor casing to capture vibrational signatures with high sensitivity. To monitor stability at 20 °C and prevent overheating as a confounding failure mode, an LM35 digital temperature sensor was attached to the BLDC motor. An ESC was connected to a 12 V DC power supply that was used to maintain the current required for each test run. The motor current was monitored continuously using an inline current sensor. All the sensors were connected to a National Instruments USB NI-6009 data acquisition (DAQ) system. The system operated at a sampling frequency of 1000 Hz, generating 50,000 data points per 30 min recording burst, with each experiment running

Table 1. *Equipment used in the experimental setup.*

Equipment	Model	Reference
DJI 9450 Plastic Propeller	Model 9450	17
DAQ System	National Instruments USB NI-6009	18
Piezoelectric Vibration Sensor	Metra KS48C	19
BLDC Motor	A2212 – 920 KV	20
Temperature Sensor	LM35	21

until propeller functional failure occurred for a total monitored duration of approximately 40 h.

3.2. Experimental Uncertainty Analysis. Quantifying the measurement uncertainty is essential for assessing the reliability of the collected degradation data and the validity of the derived prognostic features. The piezoelectric accelerometer (Metra KS48C) was factory-calibrated with a stated sensitivity tolerance of ±5% and a frequency response linearity of ±1 dB over the 1–5000 Hz operating range, which encompasses the fundamental motor rotational frequency and its harmonics. The inline current sensor was calibrated against a reference-grade digital multimeter (Fluke 87V, accuracy ±0.05% of reading) before each experimental run, yielding a measurement accuracy of ±10 mA across the 0–5 A operating range. The LM35 temperature sensor has a manufacturer-specified accuracy of ±0.5 °C at 25 °C, which is sufficient for the temperature stability monitoring purpose of maintaining the 20 °C setpoint.

The National Instruments USB NI-6009 DAQ system provides 14-bit resolution analog-to-digital conversion with a maximum absolute accuracy of ±7.73 mV at the ±10 V input range (single-ended). At the 1000 Hz sampling rate used in this study, the Nyquist frequency of 500 Hz was well above the expected vibration spectral content of the motor–propeller assembly, thereby preventing aliasing artifacts. Timing uncertainty in the DAQ clock was specified at ±50 ppm, which introduced a negligible error of less than 0.1 s over the 30 min recording burst duration. The combined expanded uncertainty (at 95% confidence, $k = 2$) for the vibration RMS feature, propagated through the RMS calculation from the accelerometer and DAQ system uncertainties, was estimated at ±6% of the measured RMS value. For the motor current RMS, the combined expanded uncertainty was ±3%. These uncertainty bounds are substantially smaller than the observed signal changes between the healthy and degraded states, which typically exceed 200% for vibrations and 30% for currents, thereby confirming that the observed degradation trends are well above the measurement noise floor and that the comparative conclusions drawn between the two sensor modalities are robust.

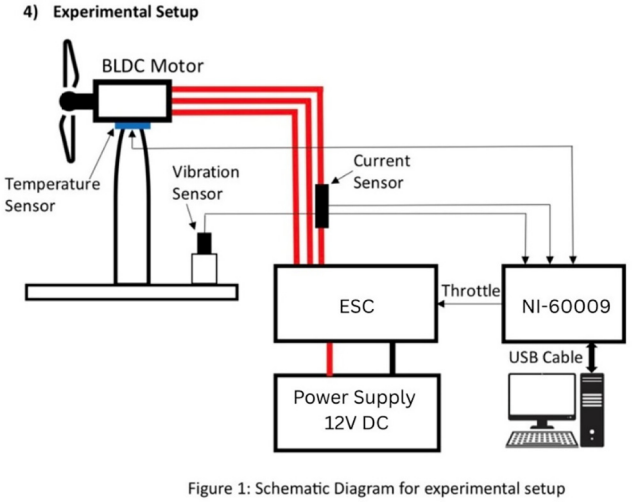

Figure 3. Schematic of the run-to-failure experimental setup

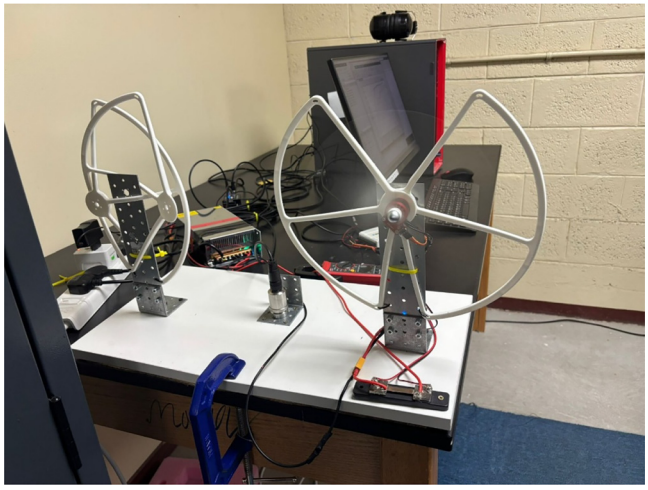

Figure 4. Photograph of the assembled testbed showing the BLDC motor, propeller, sensors, and DAQ system

3.3. Dataset Overview. An overview of the raw vibration and current signals obtained during each of the five run-to-failure tests is presented in Figures 5–9. Timestamps were used to reconstruct the true elapsed operational timeline for each dataset, which consisted of several recording bursts separated by brief idle intervals. The signals followed a consistent pattern: an initial quasi-stationary period reflecting healthy operation, progressively increasing signal amplitude and variability as structural degradation developed, culminating in a rapid escalation immediately preceding functional failure. Although the run-to-run variability in the onset and rate of degradation reflects the stochastic nature of fatigue crack initiation in composite propeller blades, this pattern was consistent across all five runs, thereby confirming the reproducibility of the experimental protocol.

The failure criterion for terminating each run was defined as the onset of functional failure, identified by a sudden and irreversible increase in the vibration amplitude accompanied by audible structural distress (cracking or fracturing sounds), at which point the motor was immediately shut down for safety. A post-test inspection of each propeller specimen confirmed visible structural damage consistent with fatigue-driven crack propagation, including edge fractures and surface delaminations.

The raw data preprocessing pipeline proceeded as follows: (1) raw voltage signals from the DAQ system were converted to physical units (m/s^2 for acceleration, A for current) using the calibrated sensor sensitivities; (2) each 30 min recording burst was segmented and its RMS value computed over the full 50,000-sample window; (3) timestamps embedded in the acquisition

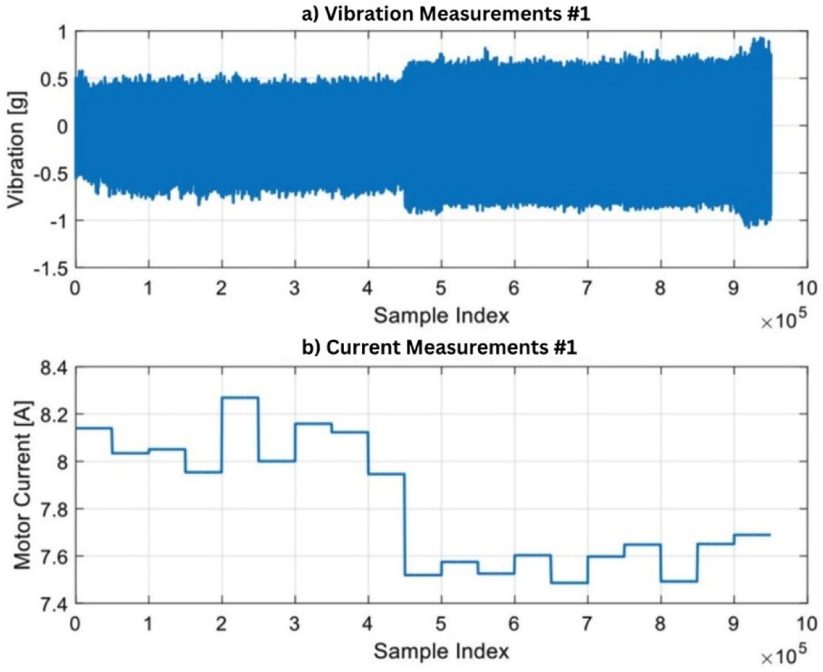

Figure 5. Overview of Dataset 1: vibration (a) and motor current (b) over the full run-to-failure duration

files were used to reconstruct the true elapsed operational timeline, accounting for idle intervals between bursts; and (4) the resulting time-ordered RMS sequences were used as input to the trendability and prognosability analyses.

The complete dataset, including all five run-to-failure experiments with raw vibration acceleration and motor current time series, is publicly available in the IEEE DataPort repository under the title "UAV Propulsion System Run-to-Failure Degradation Dataset Under Arid Conditions" (DOI: to be assigned upon acceptance). Each dataset file contains timestamped sensor readings in the CSV format, thereby enabling full reproducibility of the analyses presented in this study.

4. RESULTS AND DISCUSSION

The raw time series illustrated in Figures 5–9 of the vibration and current confirm that both sensor modalities respond to propeller degradation but differ substantially in the clarity and consistency

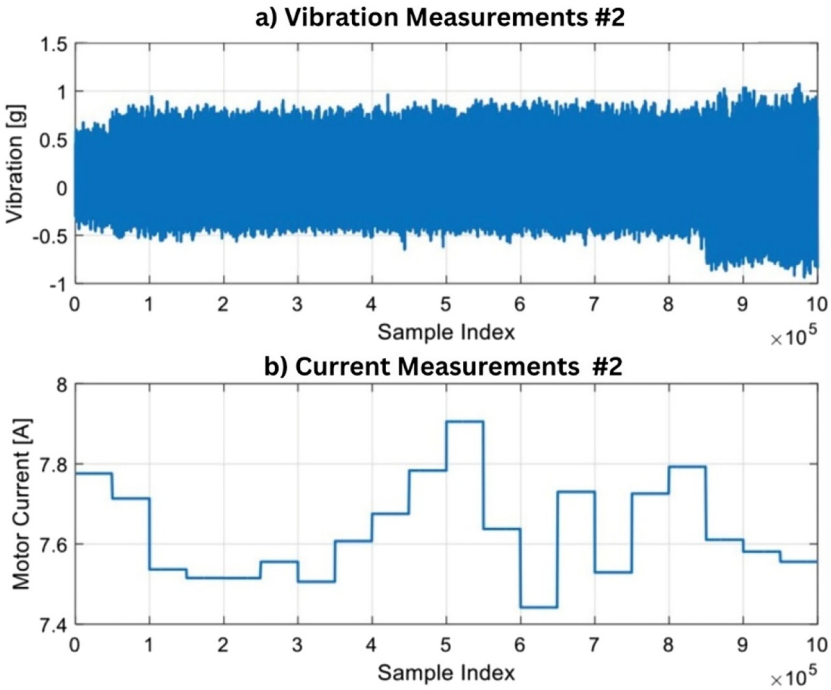

Figure 6. Overview of Dataset 2: vibration (a) and motor current (b) over the full run-to-failure duration

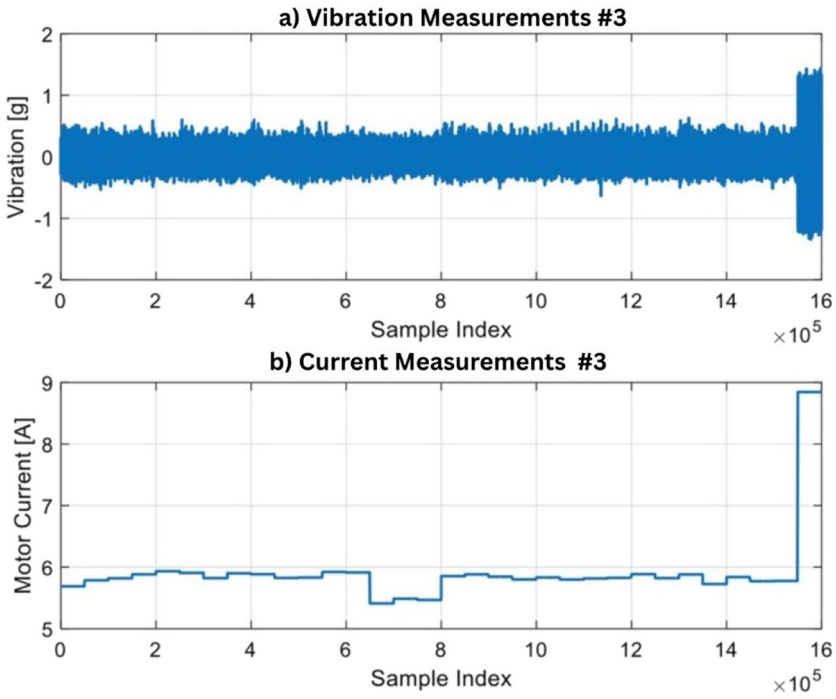

Figure 7. Overview of Dataset 3: vibration (a) and motor current (b) over the full run-to-failure duration

of the degradation signature. Visual inspection alone is insufficient to quantify the degradation tracking potential. Therefore, statistical analysis using trendability and prognosability metrics was applied to the shot-level RMS features derived from each sensor.

4.1. Trendability Analysis. Trendability examines whether a quantitative RUL estimate is supported by a consistent temporally ordered pattern in the RMS characteristics of each sensor. The strength of the linear relationship between the RMS and elapsed time was measured using the Pearson correlation. The Spearman rank correlation is more physically informative because it captures any monotonic relationship, including the nonlinear acceleration of the damage characteristic of fracture mechanics-governed crack propagation. Furthermore, it initially slowed during the crack initiation phase and then accelerated nonlinearly as the crack tip stress intensity factor increased. The shot-level RMS provides direct physical mapping from the

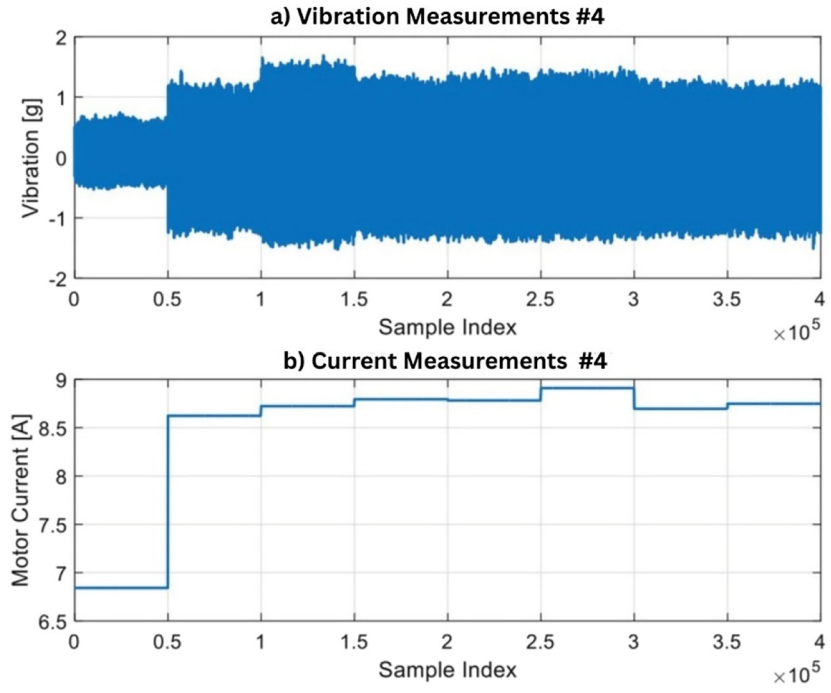

Figure 8. Overview of Dataset 4: vibration (a) and motor current (b) over the full run-to-failure duration

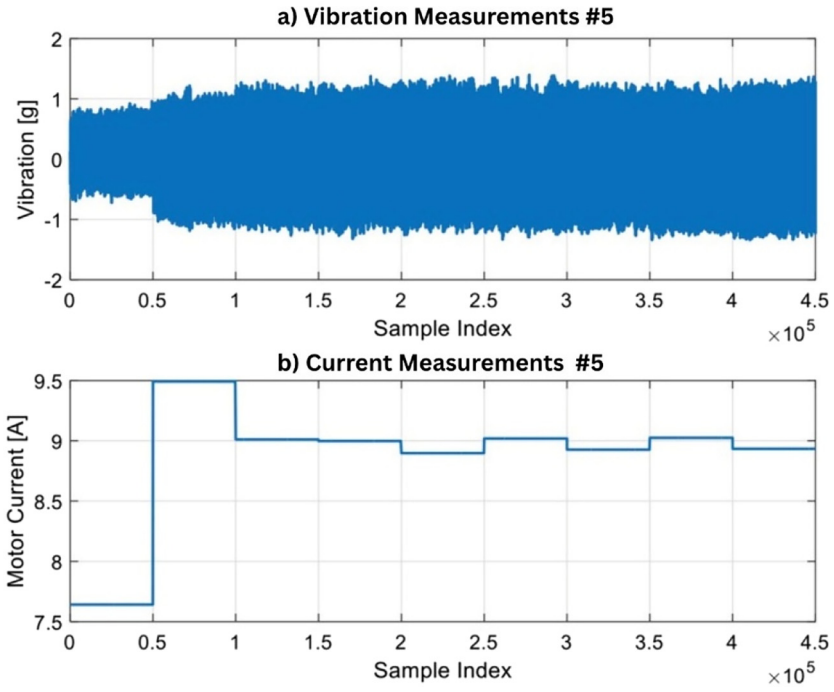

Figure 9. Overview of Dataset 5: vibration (a) and motor current (b) over the full run-to-failure duration

elapsed time to the structural health state by combining the energy content of every recording burst into a single scalar.

As shown in Figure 10, the vibration RMS consistently achieved a higher Spearman correlation with the elapsed time than the current RMS across all runs. This is physically compatible with the direct mechanical relationship between the blade structural damage and vibrational energy output. As surface flaws and propeller asymmetry build up, the aerodynamic imbalance corresponds to a quantifiable increase in the accelerometer output. Owing to the closed-loop speed regulation of the motor, which partially compensates for the propeller efficiency losses by adjusting the current draw, thereby attenuating the degradation signature in the current signal, the motor current trendability is lower and more variable across runs.

4.2. Prognosability Analysis. The statistical separability between early- and end-of-life RMS distributions is quantified by prognosability, which determines whether a sensor measurement can accurately detect failure proximity[16,17]. For vibrations, the physical basis of high prognosability is the nonlinear amplification of vibrational energy as the damage approaches a critical level. In fracture mechanics, as the crack length increases, the

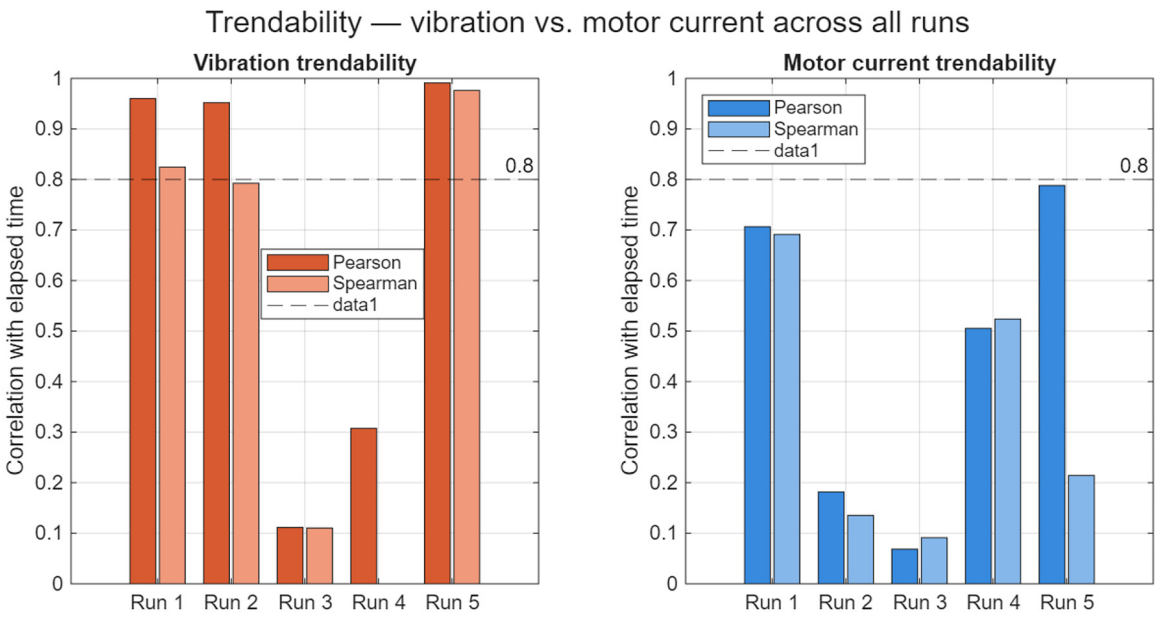

Figure 10. Trendability scores (Pearson and Spearman) for the vibration and motor current RMS values across all five run-to-failure datasets

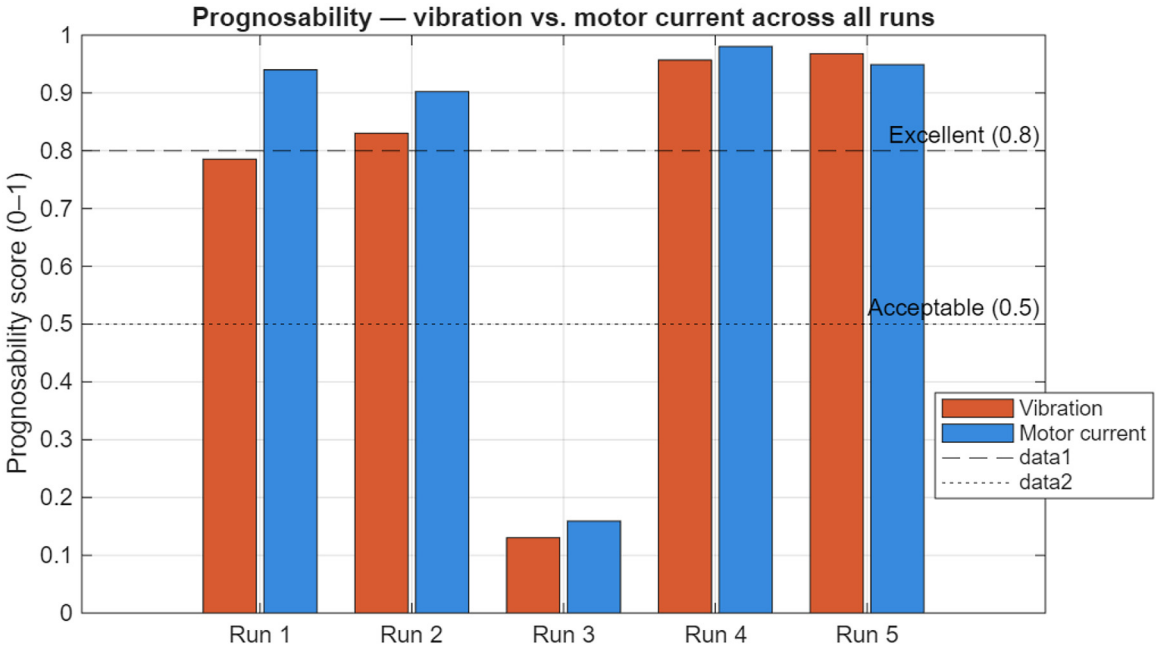

Figure 11. Prognosability scores for vibration RMS and motor current RMS across all five run-to-failure datasets

stress intensity at the crack tip increases, and the energy release rate accelerates as the crack approaches the critical length for unstable propagation. This results in well-separated distributions and a high prognosability score because the vibration RMS values in the last stage of the life of a propeller are significantly and consistently greater than those in the early stages. For the motor current, the separation is smaller and noisier because the motor controller adjusts the current to maintain speed. This compensation reduces the visible effect of degradation, rendering the changes in the current signal less clear as an indicator.

Figure 11 confirms that vibration RMS achieves better separation between the early- and end-of-life distributions than the motor current RMS across most experimental runs. This emphasizes the conclusion of the trendability analysis, which states that vibration acceleration is a more reliable indicator of propulsion system degradation for both temporal tracking and end-of-life identification. Nevertheless, the motor current provides complementary information through a trendability-based weighting approach and a sensor-fusion approach that combines both modalities, thereby enhancing the overall reliability and robustness of the prognostic systems.

5. CONCLUSIONS

This study examined the degradation tracking potential of vibration acceleration and motor current measurements across five drone propeller run-to-failure experiments using trendability and prognosability metrics. Based on the results, the following conclusions were drawn:

- Vibration acceleration consistently demonstrated superior performance compared to the motor current across both evaluation criteria. This is attributed to its direct mechanical coupling with the irreversible progression of blade damage. In contrast, the motor current signals are influenced by the closed-loop control system of the drone, which can partially compensate for the degradation and obscure its true effects.
- The observation of Spearman trendability outperforming Pearson trendability in multiple runs confirmed that the propeller degradation did not follow a constant-rate linear model. Instead, it aligns with the non-linear progression expected from fracture mechanics. This finding reinforces the use of the vibration RMS as a physically meaningful prognostic feature.
- Despite its lower performance relative to vibrations, the motor current retains its complementary diagnostic value. Therefore, a trendability-weighted sensor-fusion approach that combines both modalities is recommended to enhance the robustness of operational deployment scenarios.
- Finally, the shot-based feature extraction method developed in this study addresses a common limitation of real-world drone monitoring by reconstructing the actual operational timeline from timestamped recording bursts, thereby enabling highly accurate degradation tracking.

Future research will extend the experimental protocol to incorporate more severe environmental stressors, including elevated ambient temperatures and controlled sand particle exposure, which are representative of the Arabian Peninsula field conditions. Furthermore, machine learning algorithms for automated RUL prediction will be developed and validated using the datasets generated in this study to enable real-time prognostic capabilities for deployed UAV systems.

AFFILIATIONS AND AUTHOR DETAILS

Undergraduate Author

Lujain Almuzaini – *Aerospace Engineering Department, King Fahd University of Petroleum & Minerals, Dhahran 31261, Saudi Arabia;* 0009-0000-4104-020X
Email: s202354830@kfupm.edu.sa

Corresponding Author

Mohammed A. A. Ismail – *Research Mentor, Assistant Professor, Aerospace Engineering Department, King Fahd University of Petroleum & Minerals, Dhahran 31261, Saudi Arabia*; 0000-0002-2077-0681
Email: mohamed.ismail@kfupm.edu.sa

ACKNOWLEDGEMENTS

This study was partially supported by the Project No. INAE2404, funded by the Interdisciplinary Research Center for Aviation and Space Exploration, King Fahd University of Petroleum & Minerals, Dhahran 31261, Saudi Arabia.

REFERENCES

(1) Alotaibi, N. et al. Elevating Healthcare: Rapid Literature Review on Drone Applications for Streamlining Disaster Management and Prehospital Care in Saudi Arabia. *Healthcare* 11, 1575 (2023).

(2) Alwateer, M., Lari, S. & Woodward, B. Emerging Drone Services: Challenges and Societal Issues in Saudi Arabia. *Int. J. Adv. Comput. Sci. Appl.* 11(10), 491–498 (2020).

(3) Andrioaia, D. et al. Finding Fault Types of BLDC Motors within UAVs using Machine Learning Techniques. *Heliyon* 10, e30251 (2024).

(4) Ambroziak, L., Ołdziej, D. & Koszewnik, A. Multirotor Motor Failure Detection with Piezo Sensor. *Sensors* 23, 1048 (2023).

(5) Puchalski, R. et al. PADRE – A Repository for Research on Fault Detection and Isolation of Unmanned Aerial Vehicle Propellers. *J. Intell. Robot. Syst.* 110, 74 (2024).

(6) Ismail, M. A., Elshaar, M. E., Abdallah, A. & Quan, Q. DronePropA: Motion Trajectories Dataset for Defective Drones. *Data Brief* 60, 111589 (2025).

(7) Zahra, N. et al. Predictive Maintenance with Neural Network Approach for UAV Propulsion Systems Monitoring. in *Proc. American Control Conference (ACC)* 1–6 (2021).

(8) Sadeghzadeh, I. & Zhang, Y. A Review on Fault-Tolerant Control for Unmanned Aerial Vehicles (UAVs). in *Proc. Infotech@Aerospace 2011* (AIAA, 2011).

(9) Petritoli, E., Leccese, F. & Ciani, L. Reliability Assessment of UAV Systems: A Survey. *Sensors* 24, 6557 (2024).

(10) Puchalski, R. & Giernacki, W. UAV Fault Detection Methods, State-of-the-Art. *Drones* 6, 330 (2022).

(11) Petritoli, E., Leccese, F. & Ciani, L. Reliability and Maintenance Analysis of Unmanned Aerial Vehicles. *Sensors* 18, 3171 (2018).

(12) Elshaar, M. E. et al. UAV Propeller: Fault Detection, Characterization, and Calibration: A Comprehensive Study. *IEEE Access* 13, 187564–187583 (2025).

(13) Elshaar, M. E., Ismail, M. A., Abdullah, A. M. & Quan, Q. Fault Diagnosis of Drone Propellers Using Inner Loop Dynamics. in *Proc. 2025 Int. Conf. Control, Automation and Diagnosis (ICCAD)* 1–6 (2025).

(14) Lei, Y. et al. Machinery Health Prognostics: A Systematic Review from Data Acquisition to RUL Prediction. *Mech. Syst. Signal Process.* 104, 799–834 (2018).

(15) Zhang, W., Yang, D. & Wang, H. Data-Driven Methods for Predictive Maintenance of Industrial Equipment: A Survey. *IEEE Syst. J.* 13, 2213–2227 (2019).

(16) Coble, J. & Hines, J. W. Identifying Optimal Prognostic Parameters from Data: A Genetic Algorithms Approach. in *Annual Conference of the PHM Society* vol. 1 (2009).

(17) Hub360. DJI 9450 Plastic Propeller (Model 9450). Available at: hub360.cc/shop/0939-9450-propeller-10841 (accessed 2026).

(18) National Instruments. USB-6009 Multifunction I/O Device, Specifications. Available at: ni.com/docs/en-US/bundle/usb-6009-specs (accessed 2026).

(19) Metra Mess- und Frequenztechnik. Piezoelectric Vibration Sensor KS48C. Available at: mmf.de/produkt/ks48c (accessed 2026).

(20) Haws Work. A2212 Brushless DC Motor, 920 KV. Available at: haws-work.com/products/a2212-brushless-motor (accessed 2026).

(21) Futurlec. LM35DZ Precision Centigrade Temperature Sensor. Available at: futurlec.com/Linear/LM35DZ.shtml (accessed 2026).